Solid State Ionics 321 (2018) 62–68

Contents lists available at ScienceDirect

Solid State Ionics

journal homepage: www.elsevier.com/locate/ssi

Phenomenological model of a solid electrolyte NO_x and O_2 sensor using temperature perturbation for on-board diagnostics

Masoud Aliramezani[a,*], Charles Robert Koch[a], Ron Patrick[b]

[a] Mechanical Engineering Department, University of Alberta, Edmonton T6G 1H9, Canada
[b] ECM, Los Altos, CA 94023, USA

ARTICLE INFO

Keywords:
On-board diagnostics (OBD)
O_2 sensor
Amperometric NO_x sensor
Diesel engine

ABSTRACT

Amperometric NO_x sensors are increasingly used in automotive industry to meet the stringent emission measurement regulations. These sensors measure O_2 and NO_x concentration using two different sensing cells. In this work, a physics-based model was developed and then employed to predict the sensor output for oxygen as a function of sensor temperature and oxygen concentration. A temperature perturbation method was also developed based on the model to calibrate the sensor output with respect to oxygen concentration. The model accurately matched the experimental results for steady state and transient conditions. A two step sensor diagnostics procedure based on the sensor temperature perturbation method was then proposed. The first diagnostics step evaluates the sensor output to check if it is within the acceptable range. The second diagnosis step checks the plausibility of the sensor output based on the physics based model and temperature perturbation. A self-calibration procedure was also implemented inside the diagnostics procedure using temperature perturbation at *engine-off*. This self-recalibration only requires an external relative humidity measurement.

1. Introduction

Production NO_x and O_2 sensors are used in the automotive industry for on-board measurement of NO_x concentration in exhaust gas [1]. These sensors are typically Zirconia-based amperometric sensors manufactured using the planar zirconia multilayer technology [2-4]. The small size, fast response, short light-off time and low price make Zirconia-based amperometric NO_x and O_2 sensors ideal for commercial combustion engines [5-7]. Amperometric NO_x sensors simultaneously measure the O_2 and NO_x concentration [8].

High NO_x and particulate matter emissions are challenges to meet emission standards with Diesel engines [9-11]. Selective Catalytic Reduction (SCR) system [12, 13], Exhaust Gas Recirculation (EGR) [13, 14] and Low Temperature Combustion (LTC) [15, 16] are the most effective methods to reduce NO_x emissions. Real-time measurement of the actual NO_x concentration has become essential for engine combustion control and urea injection control of SCR systems [17, 18].

According to the stringent emission regulations [19, 20], any fault in any emission-relevant device must be detected and reported through on-board diagnostics (OBD) [21]. The first OBD standard was passed into law in 1970 by US Congress to reduce the adverse effect of vehicular emissions on environment [22]. In 1996, an updated standard (OBD II) was introduced. OBD II standard mandates monitoring of any electronic powertrain system or component that provides input to, or receives commands from the electronic control unit (ECU) [21].

Exhaust gas sensors are used upstream and/or downstream of aftertreatment systems to monitor their efficiency and performance [22-24]. To meet increasingly stringent emission standards, the accuracy of the emission sensors also needs to be increased [25-29]. This requires reliable on-board diagnostics of emission sensors in addition to the other aftertreatment components. Reliable physics-based diagnostics strategies require understanding of the sensor performance. To do this, a phenomenological sensor model is developed.

The diffusion of exhaust gas species through the sensor diffusion barriers and the electrode reactions inside the sensor chambers are the main processes that affect the sensor outputs [30, 31]. Typically, at the sensor operating condition, the diffusion of species through the barriers into the sensor chambers is the rate determining step since the diffusive flow is much slower than the sensor reaction dynamics [32]. An amperometric NO_x sensor has two main chambers that are used to measure O_2 and NO_x concentrations. In the first chamber O_2 is reduced and pumped out with a pumping current that is proportional to oxygen concentration. The remaining species then diffuse into the second chamber where NO_x is reduced. The oxygen ions from NO_x are pumped out to the third chamber (reference chamber) with a pumping current proportional to NO_x concentration.

* Corresponding author.
E-mail address: aliramez@ualberta.ca (M. Aliramezani).

https://doi.org/10.1016/j.ssi.2018.04.004
Received 15 February 2018; Received in revised form 2 April 2018; Accepted 4 April 2018

The diffusion of species through the sensor barriers and the electrode reactions of species both depend on the sensor temperature [33, 34]. The dominant diffusion mechanism of the diffusive flow inside the sensor is normal multi-component diffusion [33].

The remainder of this paper has sections on sensor modeling, model validation and an in-use temperature perturbation calibration method. The sensor output to oxygen is predicted as a function of sensor temperature and oxygen concentration with normal diffusion taken to be the dominant diffusion mechanism through the sensor barriers. Then a two step sensor diagnostics strategy is proposed to evaluate sensor output validity and plausibility by varying the sensor temperature. The model results match the experiments in transient and steady state conditions. Finally, a self-calibration method is developed based on temperature perturbation and an external relative humidity measurement.

2. Sensor model

2.1. Sensor working principle

An amperometric NO_x sensor consists of two measuring chambers to measure O_2 and NO_x concentration [33]. Exhaust gas species diffuse through the first diffusion barrier to the first chamber as schematically shown in Fig. 1. A zirconia based Nernst cell, pumps out O_2 from the first chamber with a pumping current (I_{P_1}) that is proportional to O_2 concentration in the environment. All NO_2 is reduced to NO on the electrode located in this chamber. This makes it possible to measure NO_x concentration in the second chamber. This work focuses on the first chamber of a NO_x sensor which functions as an amperometric O_2 sensor. Therefore, all the results and discussions are also relevant for an amperometric O_2 sensor.

Typically the reduction rate of species in the first chamber is much faster than the diffusive flow of species through the diffusion barrier [32, 33]. Therefore, the sensor pumping current for O_2 is proportional to the diffusion rate of O_2.

As each oxygen molecule transfers 4 electrons into the cavity, the pumping current is:

$$I_{p_1} = 4F \times \dot{n}_{diff,O2} \tag{1}$$

where, $\dot{n}_{diff,O2}$ is the diffusive molar flux of oxygen through the first diffusion barrier. The effect of NO_2 reduction to NO is neglected in Eq. (1) since NO_2 concentration is typically almost 3 orders of magnitude lower than O_2 concentration during Diesel engine operation [35].

2.2. Diffusion of exhaust gas species through the sensor

The relative mass flux (j) of species i (j_i) is calculated using Fick's law [36]:

$$j_i = -\rho D_i \frac{d\phi_i}{dx} \tag{2}$$

where, ρ, and ϕ_i are mean density and concentration of species i respectively. Normal multi-component diffusion has been found to be the dominant diffusion mechanism of species through the diffusion barriers of this type of sensor [33]. The diffusion coefficient D_i is calculated using mixture averaged method and Fuller correlation for normal multi-component diffusion [36]:

$$D_i = \frac{1 - \omega_i}{\sum_{q \neq i}^{N} \frac{x_q}{D_{iq}}} \tag{3}$$

where, x_q is mole fraction of species q and N is the number of species. The term D_{iq} is:

$$D_{iq} = \frac{10^{-3} T^{1.75} \left(\frac{1}{M_i} + \frac{1}{M_q}\right)^{1/2}}{P\left[(\Sigma\nu)_i^{1/3} + (\Sigma\nu)_q^{1/3}\right]^2} \tag{4}$$

in which, P is absolute pressure in atm, T is in K and $(\Sigma\nu)_i$ is the diffusion volume of species i, defined from [36]. The effective diffusion coefficient of the porous solid from the normal diffusion coefficient, is calculated as [32]:

$$D_{i,por} = \frac{\epsilon}{\tau} D_i$$

where ϵ is porosity and defined as: $\epsilon = \frac{V_v}{V_{total}}$, V_v and V_{total} are the void volume and the total volume of the porous media respectively and τ is tortuosity which characterizes the mean path length that a molecule has to travel within the porous media. The factor ϵ/τ is typically assumed to be constant for a given porous material [32, 37].

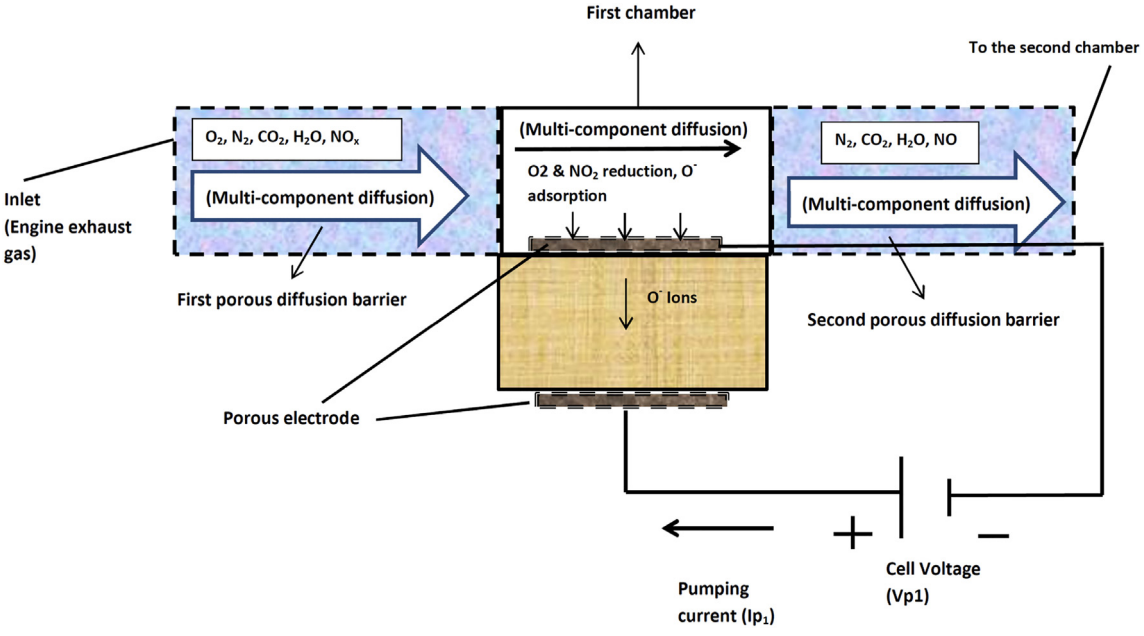

Fig. 1. Working principle and boundary condition of the first chamber of NO_x sensor (an O_2 sensor).

2.3. Sensor output as a function of temperature and O_2 concentration

Combining Eqs. (1), (2), (4), using ideal gas law and assuming all oxygen is immediately pumped out from the first chamber ($\phi_{O_2}|_{1st\ chamber} \approx 0$), results in: $I_{P_1} \propto T^{0.75}$ and $I_{P_1} \propto \phi_{O_2}$. Where, ϕ_{O_2} is O_2 concentration in the surrounding gas. Therefore:

$$I_{p_1}(T, x_{O_2}) = \overbrace{k \times T^{0.75}}^{K} \times \phi_{O_2} \tag{5}$$

in which, k is a constant and K is the slope of the linear function of I_{P_1} versus ϕ_{O_2}. At a constant O_2 concentration ($\phi_{O_{2,0}}$, reference concentration), if the sensor temperature changes from T_1 to T_2, the current ratio $\frac{I_{P_1}(T_2)}{I_{P_1}(T_1)}$ is:

$$\frac{I_{p_1}(T_2, \phi_{O_{2,0}})}{I_{p_1}(T_1, \phi_{O_{2,0}})} = \frac{k \times T_2^{0.75} \times \phi_{O_{2,0}}}{k \times T_1^{0.75} \times \phi_{O_{2,0}}} = \left(\frac{T_2}{T_1}\right)^{0.75}$$

The change in pumping current between condition two (at T_2) and condition one (at T_1) is:

$$\begin{aligned}\Delta I_{P_1}|_{\phi_{O_{2,0}}} &= I_{p_1}(T_2, \phi_{O_{2,0}}) - I_{p_1}(T_1, \phi_{O_{2,0}}) \\ &= k \times T_2^{0.75} \times \phi_{O_{2,0}} - k \times T_1^{0.75} \times \phi_{O_{2,0}} \\ &= k \times \phi_{O_{2,0}} \times T_1^{0.75} \times \left[\left(\frac{T_2}{T1}\right)^{0.75} - 1\right]\end{aligned}$$

with

$$k = \frac{\Delta I_{P_1}|_{\phi_{O_{2,0}}}}{\phi_{O_{2,0}} T_1^{0.75}\left[\left(\frac{T_2}{T_1}\right)^{0.75} - 1\right]}$$

and

$$K = \frac{\Delta I_{P_1}|_{\phi_{O_{2,0}}}}{\phi_{O_{2,0}} T_1^{0.75}\left[\left(\frac{T_2}{T_1}\right)^{0.75} - 1\right]} \times T^{0.75} \tag{6}$$

where, $\phi_{O_{2,0}}$ is the reference O_2 concentration and $\Delta I_{P_1}|_{\phi_{O_{2,0}}}$ is the change in pumping current due to temperature at a given oxygen concentration.

In normal operation, the sensor temperature is kept constant using a temperature controller that measures sensor temperature by measuring ohmic resistance of the reference Nernst cell [33]. This, according to Eq. (5), results in I_{P_1} being linearly dependant to changes in ϕ_{O_2}. The slope of the linear I_{P_1} function vs ϕ_{O_2} (K) is calibrated by the sensor manufacturer. To do this, external measurements of O_2 via a reference measurement system for at least two O_2 concentrations are needed. This relation varies from sensor to sensor due to manufacturing tolerances and sensor aging. Alternatively, the slope K can be calculated using the temperature perturbation method using only one O_2 concentration. This is schematically shown in Fig. 2. Since only one O_2 concentration is needed and the temperature can be changed using the sensor heater electronics, the sensor can be recalibrated any time there is a known oxygen concentration - for example at *engine-off* condition (ambient oxygen concentration). This recalibration can be used to remove the effect of mass production variation between different sensors or sensor aging when necessary. In addition, the methodology will be used to develop a sensor diagnostics strategy.

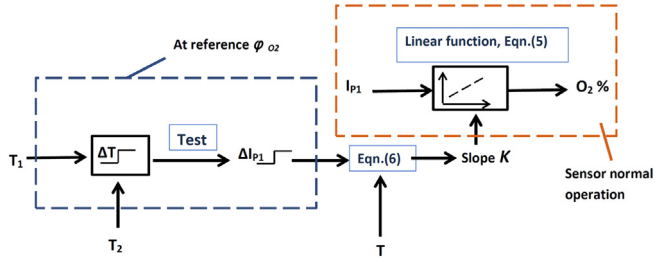

Fig. 2. I_{P_1} vs O_2 linear function calibration using temperature perturbation.

3. Experimental setup

The experiments were carried out using a production ECM O_2 - NO_x sensor (P/N: 06-05) and the corresponding control module (Fig. 3a) connected to a computer via *Kvaser Light HS* CAN interface. The sensor and control module characteristics are listed in Table 1. The sensor was located in the exhaust pipe (0.30 m upstream of the diesel oxidation catalyst) of a 4 cylinder medium duty Cummins QSB 4.5 160 - Tier 3 diesel engine, (Fig. 3b) which is connected to a Dyne Systems 1014 W passive eddy current dynamometer. The stock engine controller controls engine speed and the dynamometer controller maintains the user specified load torque on the engine. The engine characteristics are listed in Table 2.

To check for a valid sensor output, the *engine-off* condition was taken as the reference point and all tests have been carried out at *engine-off*. At this condition the sensor O_2 concentration is known and is not a function of engine operating condition or fuel type. Engine fuel cut-off condition that takes place during long downhill gradients [39], could also be used as the reference point in vehicle operation.

At *engine-off* condition, the sensor is exposed to local atmospheric pressure (≈ 94 kPa) and room temperature (19 ° C); however, the sensor performance is not affected by the environment temperature as the sensor control module shown in Fig. 3a controls the sensor temperature by controlling the heater power mounted inside the sensor. The impedance of the reference Nernst cell (R_{pvs}) varies with sensor temperature and this was used to measure and control the sensor temperature.

4. Results and discussion

4.1. Model validation

A heat transfer model developed in [33] was used to define sensor temperature as a function of R_{pvs} as:

$$T = c_1 (R_{pvs})^{c_2} \tag{7}$$

where T is temperature in K and R_{pvs} is the impedance of the reference Nernst cell in Ohms. For this sensor $c_1 = 1396$, $c_2 = -0.0559$ are determined using a *nonlinear least squares* fit [40] with a squared correlation coefficient of $R^2 = 0.991$.

Eq. (7) was used to calculate sensor temperature from R_{pvs} during the steady state and transient tests. The sensor temperature calculated by a heat transfer model [33] is compared to the correlation in Eq. (7) versus R_{pvs}, shown in Fig. 4 (a), with the residuals shown in Fig. 4 (b). The temperature model has maximum error of 6.25 K (0.58%) at $R_{pvs} =$ 100 Ω (T = 1086 K) as shown in Fig. 4. The model error first decreases by increasing R_{pvs} and then increases to 4.2 K (0.43%) at $R_{pvs} =$ 660 Ω (T = 975 K).

A temperature perturbation test around the sensor normal operation temperature was performed to evaluate the model accuracy for the rising and falling temperature steps. The test was carried out at *engine-off* with the standard $T = 1023$ K as the reference sensor temperature. The sensor output at all other sensor temperatures were defined based on the reference output at $T = 1023$ K using Eq. (5). The transient and steady state results of the perturbation test are shown in Fig. 5 which shows a comparison of desired temperature versus the sensor temperature calculated from (Eq. (7)). In addition, a comparison of model current I_{p_1} (Eq. (5)) versus experiment for step changes in set point temperature is also shown in Fig. 5.

The model is capable of accurately simulating the effect of temperature perturbation on the sensor output in steady state and transient condition as shown in Fig. 5. The overshoot and undershoot in sensor output shown in Fig. 5 are caused by the overshoot and undershoot of

(a) ECM NOx sensor and the control module

(b) Diesel Engine, Dynamometer and exhaust system

Fig. 3. Experimental setup.

Table 1
O_2 - NO_x sensor and module characteristics [38].

NO_x measurement range	0 to 5000 ppm
O_2 measurement range	0 to 25%
NO_x measurement accuracy	± 5 ppm
O_2 measurement accuracy	± 0.2%
Response time	Less than 1 s for NO_x and less than 150 ms for O_2

Table 2
Engine characteristics.

Engine type	In-line, 4-cylinder
Displacement	4.5 L
Peak torque	460 lb-ft (624 N.m) @ 1500 rpm
Peak power	165 hp (123 kW) @ 2000 rpm
Aspiration	Turbocharged and intercooler
Certification level	Tier 3/Stage IIIA

sensor temperature control as shown in Fig. 5. The maximum overshoot and undershoot in sensor output were 12.8% and 8.8% respectively with the maximum *"2% settling time"* of 14.6 s. It should be noted that the temperature controller is designed for regulating the temperature at T = 1023 K and is not tuned for steps in sensor temperature, so the overshoot is expected. This can be seen by comparing the actual temperature to the set point temperature. This difference can be significantly reduced by tuning the temperature controller parameters on the sensor control module.

With $T_1 = 1010$ K and $\phi_{O_2,0} = 20.7$ %, $\Delta I_{P_1}|_{\phi_{O2,0}} = +0.105$ (mA) for $\Delta T = +45$ K the parameter K in Eq. (6) is calculated as k = 0.1543. This point was then used as the base point to evaluate the effect sensor reference temperature and temperature step size on ΔI_{P_1}. This is shown in Fig. 6 where increasing reference sensor temperature (T_1) decreases ΔI_{P_1} for a fixed ΔT. In other words, the slope of ΔI_{P_1} vs. ΔT decreases as the sensor temperature increases and therefore, sensitivity of sensor output steps to temperature perturbation decreases by increasing sensor temperature. This conclusion is valid for the whole range of sensor operating temperatures which varies from sensor to sensor. In this range, the sensor temperature should be high enough to activate the sensor electrochemical reactions and lower than the melting point of electrodes. After the sensor temperature step, steady state is achieved for the constant values in Fig. 5.

4.2. Sensor diagnostics and self-calibration

A valid sensor output must be within a certain range defined by oxygen mole fraction in the environment. The O_2 mole fraction in the environment is a function of relative humidity in air [41]. Assuming the atmospheric air as an ideal-gas mixture with total pressure (p_a) which is the sum of the partial pressure of dry air ($p_{a,dry}$) and the partial pressure of water vapor (p_v) [41]:

$$p_a = p_{a,dry} + p_v \tag{8}$$

This shows that the partial pressure of species in humid air is less than dry air due to the partial pressure of water vapor. Therefore, O_2 mole fraction in air is [42]:

$$\phi_{O_2}(\%) = \phi_{O_2,dry}(\%) - c_h(T) \times RH \tag{9}$$

where, $\phi_{O_2,dry}$ is O_2 mole fraction in dry air ($\approx$ 20.9%) and is a weak function of environment temperature [41]. The relative humidity is *RH* and $c_h(T)$ is the temperature correction factor that increases with temperature [42]. It should be noted that the atmospheric pressure (altitude) also affects the absolute partial pressure of O_2 in the atmospheric air. However, the O_2 mole fraction in air is not affected by the atmospheric pressure. Considering the worst case scenario to be 100% relative humidity at 60°C and 101 kPa, the minimum possible value of O_2 % is 16.8% according to [41]. The maximum possible O_2 % is for dry air and is considered to be 20.9% [41]. Thus, the acceptable range for O_2 sensor output is defined based on the maximum and minimum valid values. If the sensor output is out of this range, a diagnostic can be generated to indicate that the sensor is not working properly and needs to be recalibrated or perhaps even replaced. This is a binary plausibility diagnostic of: "*working properly*" or "*problem*". The next level is a more complex diagnostic used to evaluate the sensor performance. Eq. (5) is used to estimate ΔI_{P_1} for a given ΔT ($\Delta I_{P_1(model)}$). The sensor accuracy and plausibility are evaluated by comparing the $\Delta I_{P_1(model)}$ and $\Delta I_{P_1(test)}$. The test error, e_t, is:

$$e_t = \Delta I_{P_1(test)} - \Delta I_{P_1(model)} \tag{10}$$

This is schematically shown in Fig. 7.

A variety of diagnostic tests including a model based method can be used on the system shown in Fig. 7 [43-47] but these are not the subject of this paper. A high value of e_t means that either the sensor diffusion barrier is damaged or the sensor temperature controller is not working properly. For instance, according to Eq. (5), for $\phi_{O_2,dry} = 20.7$ % and $T_0 = 976$ K, a 100°C deviation between the actual ΔT and the required ΔT, causes a 0.29 mA increase in e_t and 2% error in oxygen measurement assuming the sensor barrier is working properly. A damaged

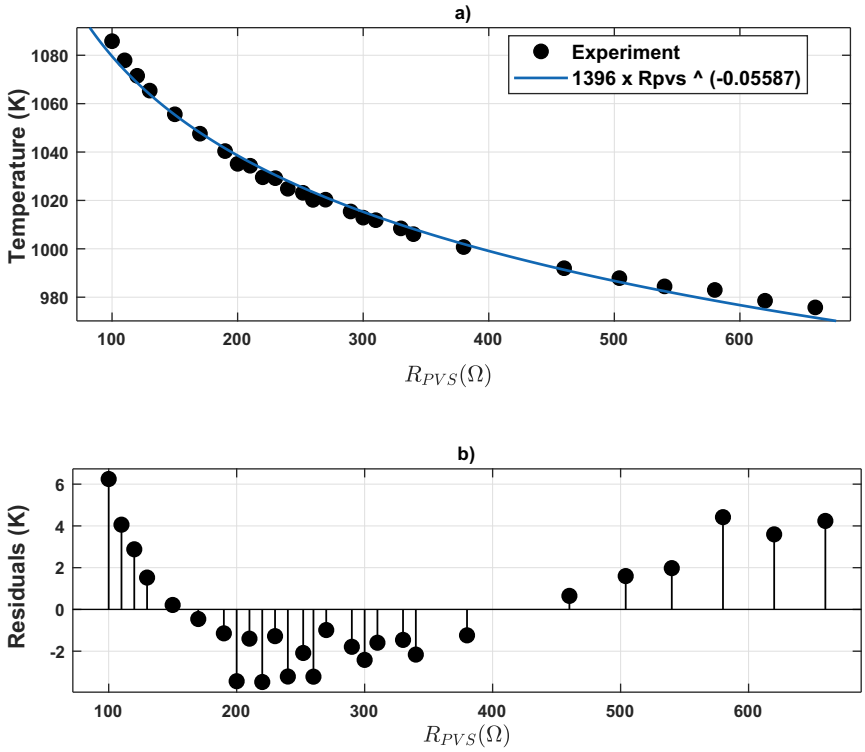

Fig. 4. a) Sensor temperature from heat transfer model [33] (symbols) and Eq. (7) correlation (line) versus Nernst Cell impedance $R_{PV\,S}$ b) Temperature error as a function of $R_{PV\,S}$.

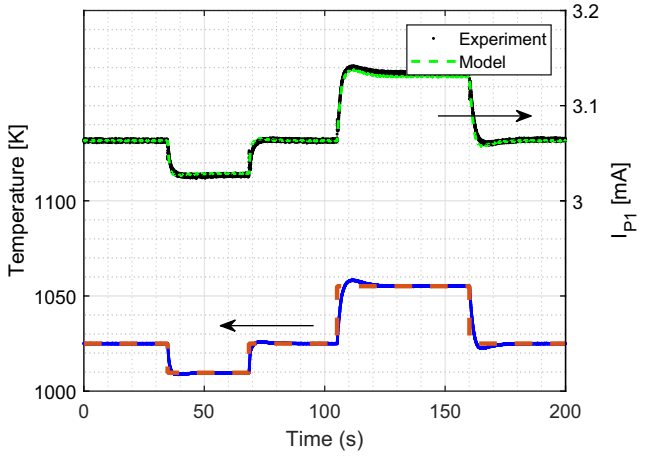

Fig. 5. Transient sensor behavior during sensor temperature perturbation test.

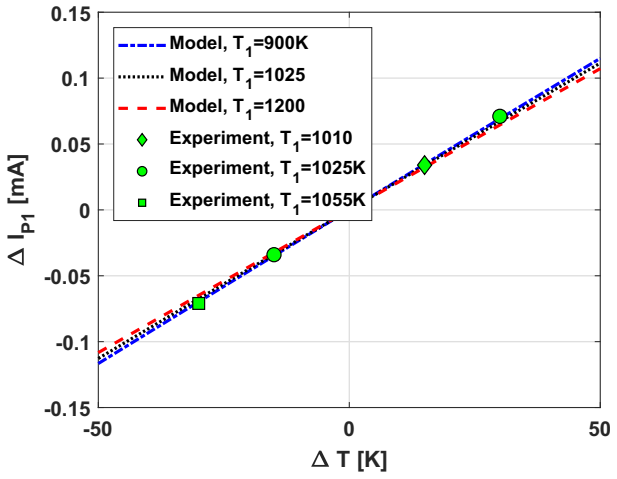

Fig. 6. The effect of temperature step size and reference temperature (T_1) on ΔI_{P_1}. Experimental results are from Fig. 5 (steady state).

diffusion barrier can cause much more deviation than this by effecting the diffusion mechanism inside the sensor. Choosing a maximum allowable error in O_2 measurement of 0.2%, the maximum value of 0.03 mA was considered for for e_t (et_{MAX} = 0.03 mA).

The effect of sensor aging can also increase e_t and this error can be nulled by re-calibrating the sensor. External measurement of relative humidity in the environment can be used to recalibrate the sensor according to Eq. (9). The proposed sensor diagnostics and recalibration strategy are shown in Fig. 8.

The first step of the sensor diagnostics is the plausibility check where the sensor output is evaluated by checking whether it is within a valid range. In the second step, the temperature perturbation test is done to calculate the error, e_t, between the expected ΔI_{p_1} from the model and the actual ΔI_{p_1} from the test result. A simple diagnostic is to see if e_t is more than $e_{t_{MAX}}$. If it is, a recalibration loop takes place to check if the error can be removed by sensor recalibration. If the error is removed in the first recalibration loop, it is assumed that the sensor is still reliable and working properly and recalibration is needed to account for minor changes in the sensor diffusion barrier characteristics. In this case, recalibrating the sensor output vs. actual oxygen concentration will increase the sensor accuracy. As mentioned, due to partial pressure of water vapor, measuring the relative humidity with an external measurement system, increases the reliability of sensor calibration. However, if the test error is higher than the limit after the first recalibration loop, then either the sensor temperature controller that includes the heater does not work properly or the sensor diffusion barrier is damaged (diagnosed) or an unknown error.

The diagnostics strategy that has been developed in this work, only monitors the first diffusion barrier and O_2 sensing cell of a NO_x sensor

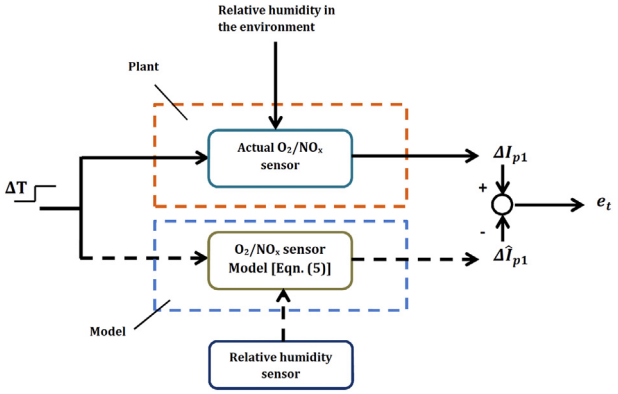

Fig. 7. Error calculation for temperature perturbation test.

as well as the performance of sensor temperature controller. This procedure makes O_2 sensor output and NO_x sensor output more reliable as both O_2 and NO_x species pass through the first diffusion barrier. However, any failure in electrochemical performance of NO_x sensing cell (second chamber) is not monitored with this diagnostics strategy and therefore it does not provide an absolute confirmation for NO_x output validity. This diagnostics is a necessary but not sufficient requirement for proper NO_x sensor operation (Table 3). If the sensor does not pass diagnostic results, neither O_2 nor NO_x output are reliable and the sensor must be replaced. Diagnostics of the electrochemical system of the NO_x sensing cell will be studied in our future work.

5. Conclusions

An on-board diagnostics strategy was developed using a physics-based model of an amperometric NO_x-O_2 sensor. The model predicts the sensor O_2 output as a function of sensor temperature and oxygen concentration based on normal multi-component diffusion mechanism of exhaust gas species through the sensor. A temperature perturbation method was proposed and used to calibrate the sensor output with respect to oxygen concentration. To evaluate the accuracy of the model in steady state and transients, temperature perturbation tests for both rising and falling sensor temperature steps are performed experimentally and the model results closely match the experiments.

A two step sensor diagnostics strategy was then proposed to evaluate the sensor output based on the sensor output validity range and a model-based diagnostics strategy that includes a temperature perturbation test. A self-calibration procedure was included in the diagnostics procedure which requires an external relative humidity measurement.

The plausibility of the sensor output as well as the performance of sensor heater and diffusion barriers can be evaluated with the proposed physics-based diagnostics strategy.

Table 3
Interpretation of the diagnostics test result.

Diagnostics result	Is O_2 output reliable?	Is NO_x output reliable?
Not passed	NO	NO
Passed	YES	Not diagnosed

Acknowledgments

This work has been partially supported by the Natural Sciences and Engineering Research Council of Canada (grant number 2016-04646) and Canada First Research Excellence Fund.

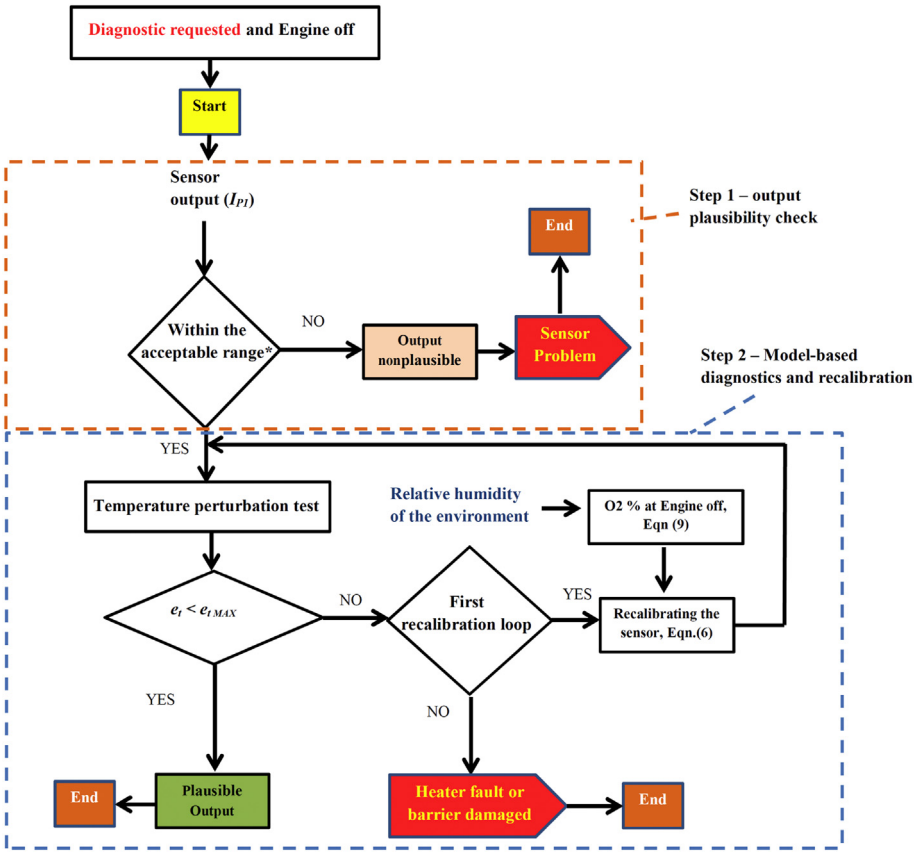

Fig. 8. Sensor diagnosis schematic (*Engine off condition*). * Acceptable output range for ϕ_{O_2} is between 16.8% and 20.9%.

References

[1] V. Betageri, R. Mahesh, Effects of the real driving conditions on the NOx emission of a medium duty diesel commercial vehicle, Symposium on International Automotive Technology 2017, SAE International, January 2017.
[2] R. Moos, A brief overview on automotive exhaust gas sensors based on electroceramics, Int. J. Appl. Ceram. Technol. 2 (5) (2005) 401–413.
[3] T. Liu, X. Zhang, L. Yuan, J. Yu, A review of high-temperature electrochemical sensors based on stabilized zirconia, Solid State Ionics 283 (2015) 91–102.
[4] G. Lu, Q. Diao, C. Yin, S. Yang, Y. Guan, X. Cheng, X. Liang, High performance mixed-potential type NOx sensor based on stabilized zirconia and oxide electrode, Solid State Ionics 262 (2014) 292–297 solid State Ionics 19 Proceedings of the 19th International Conference on Solid State Ionics.
[5] T. Ono, M. Hasei, A. Kunimoto, N. Miura, Improvement of sensing performances of zirconia-based total NOx sensor by attachment of oxidation-catalyst electrode, Solid State Ionics 175 (1) (2004) 503–506.
[6] E.L. Brosha, B.W. Chung, D.R. Brown, I.D. Raistrick, F.H. Garzon, Amperometric oxygen sensors based on dense Tb-Y-Zr-O electrodes, Solid State Ionics 109 (1) (1998) 73–80.
[7] S.I. Somov, G. Reinhardt, U. Guth, W. Gpel, Multi-electrode zirconia electrolyte amperometric sensors, Solid State Ionics 136 (Supplement C) (2000) 543–547 proceedings of the 12th International Conference on Solid State Ionics.
[8] H. Sasaki, D. Scholl, M. Parsons, H. Inagaki, K. Shiotani, J. Visser, G. Zawacki, T. Kawai, S.Teramoto, T. Kubinski, Development of an Al2O3/ZrO2-composite high-accuracy NOx sensor, SAE Technical Paper, SAE International, 04 2010.
[9] V.J. Timothy, Review of vehicular emissions trends, SAE Int. J. Engines 8 (04 2015).
[10] V. Praveena, M. Martin, A review on various after treatment techniques to reduce NOx emissions in a CI engine, J. Energy Inst. (2017).
[11] P. Geng, Q. Tan, C. Zhang, L. Wei, X. He, E. Cao, K. Jiang, Experimental investigation on NOx and green house gas emissions from a marine auxiliary diesel engine using ultralow sulfur light fuel, Sci. Total Environ. 572 (Supplement C) (2016) 467–475.
[12] B. Guan, R. Zhan, H. Lin, Z. Huang, Review of state of the art technologies of selective catalytic reduction of NOx from diesel engine exhaust, Appl. Therm. Eng. 66 (1) (2014) 395–414.
[13] M. Salazar, S. Hoffmann, L. Tillmann, V. Singer, R. Becker, W. Grunert, Hybrid catalysts for the selective catalytic reduction (SCR) of NO by NH3: precipitates and physical mixtures, Appl. Catal. B Environ. 218 (Supplement C) (2017) 793–802.
[14] R. Verschaeren, W. Schaepdryver, T. Serruys, M. Bastiaen, L. Vervaeke, S. Verhelst, Experimental study of NOx reduction on a medium speed heavy duty diesel engine by the application of EGR (exhaust gas recirculation) and Miller timing, Energy 76 (2014) 614–621.
[15] K. Ebrahimi, M. Aliramezani, C. Koch, An HCCI control oriented model that includes combustion efficiency, IFAC-PapersOnLine 49 (11) (2016) 327–332.
[16] A. Jain, A.P. Singh, A.K. Agarwal, Effect of split fuel injection and EGR on NOx and PM emission reduction in a low temperature combustion (LTC) mode diesel engine, Energy 122 (Supplement C) (2017) 249–264.
[17] M. Aliramezani, C. Koch, R. Hayes, Estimating tailpipe NOx concentration using a dynamic NOx/ammonia cross sensitivity model coupled to a three state control oriented SCR model, IFAC-PapersOnLine 49 (11) (2016) 8–13.
[18] F. Tschanz, A. Amstutz, C. Onder, L. Guzzella, Feedback control of particulate matter and nitrogen oxide emissions in diesel engines, Control. Eng. Pract. 21 (12) (2013) 1809–1820.
[19] F. Posada, A. Bandivadekar, Global overview of on-board diagnostic (OBD) systems for heavy-duty vehicles, Int. Counc. Clean Transp. (2015).
[20] Lev III Amendments to the California Greenhouse Gas and Criteria Pollutant Exhaust and Evaporative Emission Standards and Test Procedures and to the On-board Diagnostic System Requirements for Passenger Cars, Light-duty Trucks and Medium-duty Vehicles and to the Evaporative Emission Requirements for Heavy-duty Vehicles. California Air Resources Board, 2012.
[21] P. Baltusis, On board vehicle diagnostics, Convergence International Congress & Exposition On Transportation Electronics, Convergence Transportation Electronics Association, oct 2004.
[22] J. Mohammadpour, M. Franchek, K. Grigoriadis, A survey on diagnostic methods for automotive engines, Int. J. Engine Res. 13 (1) (2012) 41–64.
[23] T. Ritter, G. Hagen, J. Lattus, R. Moos, Solid state mixed-potential sensors as direct conversion sensors for automotive catalysts, Sensors Actuators B Chem. (2017).
[24] M. Andersson, P. Ljung, M. Mattsson, M. Löfdahl, A. Spetz, Investigations on the possibilities of a MISiCFET sensor system for OBD and combustion control utilizing different catalytic gate materials, Top. Catal. 30 (1-4) (2004) 365–368.
[25] A. Iio, H. Ikeda, S.A. Anggraini, N. Miura, Sensing characteristics of YSZ-based oxygen sensors attached with BaxSr1-xFeO3 sensing-electrode, Solid State Ionics 285 (Supplement C) (2016) 234–238 the 40th Symposium on Solid State Ionics in Japan.
[26] A. Osburn, C. Ferguson, T. Hall, B. Liimatta, NOx Sensor Diagnostic for an Exhaust Aftertreatment System, (June 30 2016) US Patent App. 14/586,174.
[27] C. Nagel, A. Franz, T. Pfister, Method for Checking the Plausibility of a NOx Sensor in an SCR Catalytic Converter System, (May 11 2017) US Patent App. 15/346,227.
[28] X. Gao, T. Liu, X. Zhang, B. He, J. Yu, Properties of limiting current oxygen sensor with La0.8Sr0.2Ga0.8Mg0.2O3 solid electrolyte and La0.8Sr0.2(Ga0.8Mg0.2)1-xCrxO3- dense diffusion barrier, Solid State Ionics 304 (Supplement C) (2017) 135–144.
[29] A. Hunter, Method, Apparatus, and System for Diagnosing at Least One NOx Sensor of a Diesel Engine System, (April 12 2017) EP Patent App. EP20,160,177,457.
[30] T. Nakamura, Y. Sakamoto, K. Saji, J. Sakata, NOx decomposition mechanism on the electrodes of a zirconia-based amperometric NOx sensor, Sensors Actuators B Chem. 93 (1) (2003) 214–220.
[31] N. Collings, J.A. Harris, K. Glover, Estimating IC engine exhaust gas lambda and oxygen from the response of a universal exhaust gas oxygen sensor, Meas. Sci. Technol. 24 (9) (2013) 095101.
[32] S. Regitz, N. Collings, Fast response air-to-fuel ratio measurements using a novel device based on a wide band lambda sensor, Meas. Sci. Technol. 19 (7) (2008) 075201.
[33] M. Aliramezani, C.R. Koch, R.E. Hayes, R. Patrick, Amperometric solid electrolyte NOx sensors the effect of temperature and diffusion mechanisms, Solid State Ionics 313 (Supplement C) (2017) 7–13.
[34] I.I. Soykal, P.H. Matter, L.B. Thrun, R.Q. Long, S.L. Swartz, U.S. Ozkan, Amperometric NOx sensor based on oxygen reduction, IEEE Sensors J. 16 (6) (March 2016) 1532–1540.
[35] C.P. Cho, Y.D. Pyo, J.Y. Jang, G.C. Kim, Y.J. Shin, NOx reduction and N2O emissions in a diesel engine exhaust using Fe-zeolite and vanadium based SCR catalysts, Appl. Therm. Eng. 110 (Supplement C) (2017) 18–24.
[36] J.R. Welty, C.E. Wicks, G. Rorrer, R.E. Wilson, Fundamentals of Momentum, Heat, and Mass Transfer, John Wiley & Sons, 2009.
[37] R.J. Millington, Gas diffusion in porous media, Science 130 (3367) (1959) 100–102.
[38] http://www.ecm-_co.com/product.asp?ncant.
[39] P.M. Khan, V.G. Halbe, K. Rajakumar, K.N. Manjunath, K.C. Vora, Development and evaluation of exhaust brake systems for light commercial vehicle, SIAT 2005, The Automotive Research Association of India, jan 2005.
[40] P. Teunissen, Nonlinear least squares, Manuscr. Geodaet. 15 (1990) 137–150.
[41] Y.A. Cengel, M.A. Boles, Thermodynamics: an engineering approach, Sea 1000 (2002) 8862.
[42] B. Bugbee, M. Blonquist, Absolute and relative gas concentration: understanding oxygen in air, February 27 (2006) 1–9.
[43] P.M. Frank, Analytical and qualitative model-based fault diagnosis - a survey and some new results, Eur. J. Control. 2 (1) (1996) 6–28.
[44] H. Li, Y. Gao, P. Shi, H.K. Lam, Observer-based fault detection for nonlinear systems with sensor fault and limited communication capacity, IEEE Trans. Autom. Control 61 (9) (Sept 2016) 2745–2751.
[45] R. Isermann, Supervision, Fault-detection and Fault-diagnosis Methods - A Short Introduction, Springer Berlin Heidelberg, Berlin, Heidelberg, 2017, pp. 25–47.
[46] A.B. Youssef, S.K.E. Khil, I. Slama-Belkhodja, State observer-based sensor fault detection and isolation, and fault tolerant control of a single-phase PWM rectifier for electric railway traction, IEEE Trans. Power Electron. 28 (12) (Dec 2013) 5842–5853.
[47] Z. Gao, C. Cecati, S. Ding, A survey of fault diagnosis and fault-tolerant techniquespart I: fault diagnosis with model-based and signal-based approaches, IEEE Trans. Ind. Electron. 62 (6) (2015) 3757–3767.